Influence of 3D Printing Process Parameters on the Radiation Characteristics of Dense Dielectric Lens Antennas

Fikret Tokan[1], *, Selami Demir[2], and Alper Çalışkan[1]

Abstract—In recent years, additive manufacturing has found increasing interest in the fabrication of dielectric antennas. Using additive manufacturing brings significant advantages such as design flexibility, compactness, fast and low-cost manufacturing compared to traditional fabrication methods. Dielectric antennas having dense material allow high power transfer efficiency through the lens. However, a successful 3D printing process with dense dielectric materials is a great challenge. This paper investigates the impact of main process parameters during 3D printing; namely printing speed, process temperature, and layer height on the resulted relative electrical permittivity values of dense dielectric materials. Test samples are printed with a dielectric material having $\varepsilon_{\mathbf{r}} = \mathbf{10}$, and relative permittivity variations of these samples are measured with a vector network analyzer in X-band (8.2–12.4 GHz). In this way, optimum printing parameters are determined. The influence of dielectric constants of printed materials on the antenna radiation characteristics is inspected for an extended hemispherical lens antenna by a full-wave computer-aided design tool. Results demonstrate that an additively manufactured dense dielectric antenna will act as a traditionally manufactured dielectric antenna if and only if it is manufactured with optimum printing parameters.

1. INTRODUCTION

With their high gain, compact size, and practicality, dielectric loaded lens antennas present promising solutions for beam steering applications in millimeter-wave and sub-millimeter-wave applications [1–3]. The capabilities of these antennas are investigated for automotive radar applications and passive imaging systems [4, 5]. Dielectric loaded lens antennas manufactured with dense low-loss materials provide high power transfer efficiency within the lens. Moreover, a lens antenna fabricated with dense dielectric material geometrically approximates to an elliptical lens structure [6]. However, when the relative permittivity of an antenna material is high, namely higher than three, a large number of internal reflections occur at the dielectric material-air interface [7]. The intensities of these internal reflections increase dramatically with the increase of dielectric contrast with free space. Strong internal reflections inside the antenna cause degradation in return loss, radiation efficiency, and gain [7, 8]. These undesirable reflections can be significantly reduced by placing circular corrugations on the lens outer surface using stereolithography [9–11]. Stereolithography is a high-cost high-resolution additive manufacturing (AM) technique for millimeter-wave applications [12]. Wave transformers made of artificial dielectrics are also applicable in reducing unwanted reflections [13].

In a traditional fabrication process, the most common implementation for minimizing these strong internal reflections is positioning dielectric matching layers (MLs) on top of the antenna [14, 15]. Properly designed MLs minimize internal reflections, ensure smooth energy transition to air, and consequently provide improved radiation characteristics. While a single ML is sufficient for narrowband

* Corresponding author: Fikret Tokan (ftokan@yildiz.edu.tr).

[1] Department of Electronics and Communication Engineering, Yildiz Technical University, Esenler, Istanbul 34220, Turkey.
[2] Department of Environmental Engineering, Yildiz Technical University, Esenler, Istanbul 34220, Turkey.

impedance matching [16], multiple MLs should be applied to broadband applications [8]. However, manufacturing the antenna with multiple MLs requires materials with different dielectric constants. The bonding process of MLs to antenna core material during the fabrication increases complexity and cost of the antenna. Besides, parasitic air gaps between antenna core and coating dielectric materials result in reflections inside the lens. An alternative solution is to drill holes in the upper part of dielectric lens to approximately lower dielectric constants using computerized numerical control (CNC) machines [17, 18]. Since high permittivity dielectric slabs can often be fragile during perforation process, the number and frequency of perforations are restricted to mechanical strength.

AM is recently introduced as a promising solution for prototyping of RF devices to eliminate the above-mentioned critical shortcomings. Advantages of AM include ability to design and fabricate samples much faster than traditional manufacturing processes. Besides, AM exhibits the capability to fabricate low-cost complex structures and flexibility in the choice of materials. In [19], an X-band nonuniform reflectarray antenna with Symbolic Regression is proposed. Dielectric constants of three different 3D printed dielectric materials are measured using the coaxial transmission line method [20]. In these works, standard Fused Filament Fabrication (FFF) with Polylactic Acid (PLA) materials which are not specifically produced for RF applications are utilized. These materials have low relative permittivity, $\varepsilon_r \cong 2.4$, and high dielectric loss, $\tan\delta \cong 0.02$–0.07 characteristics that deteriorate the RF system performance.

In the last decade, low-loss and high-quality low permittivity dielectric materials are fabricated for RF designs [21]. A simple, low-cost additive manufacturing technique is proposed [22] for fabricating structures compatible with high-density packaging solutions. Ceramic composite core is covered by low-loss and low-permittivity acrylonitrile-butadiene-styrene (ABS) material to enhance antenna gain. A low-cost and light weight 3D printed dielectric resonator reflectarray is presented in [23]. Composite ABS-based material, which can be smoothly extruded above $210°$, is used. Due to imperfect fabrication process, the measured gain is lower than the simulated gain in almost the whole frequency.

To provide higher power transfer efficiency, low-loss materials with relative permittivity values in the range of 4.5–11 should be utilized in the 3D printing process of dielectric antennas. However, a successful 3D printing process with dense dielectric materials is a great challenge. 3D graded index planar lenses are printed for the frequency band of 12–18 GHz [24]. Far-field radiation patterns show that measured gain is more than $2\,\mathrm{dB}$ lower than the simulated gain. A wideband 3D printed end-fire dielectric antenna is proposed in [24]. Four dielectric sections with tapered permittivities are designed to support smooth transition to free space. Tapered permittivities are obtained by varying the infill percentage of the Preperm filament, $\varepsilon_r = 10$ during 3D printing process. Fast printing settings are utilized in the work. Due to the non-optimal printing settings, relative permittivity of antenna core is measured as 8.3 rather than the expected value of 10. This can be associated with a resultant infill percentage lower than 100% due to air gaps confined within the printed volume.

Although process settings have substantial impact on the relative permittivity of printed dielectric materials, none of the studies given in [19–25] have taken the printing parameters into consideration. When fast settings are used in the fabrication process, materials generally have lower permittivities than the expected value. The discrepancy increases dramatically in high dielectric materials. While a process temperature as low as $210°\mathrm{C}$ is sufficient to extrude low permittivity materials smoothly. It is determined in [26, 27] that temperatures about $240°\mathrm{C}$ are best suited for allowing consistent extruding.

In this work, the impact of essential 3D printing parameters, namely, printing speed, process temperature, and layer height on the resultant relative permittivity values of dense dielectric Preperm ABS1000, is investigated. Test samples are printed with different settings and measured by an Anritsu Vector Network Analyzer. In this way, optimum printing settings are determined. To show the necessity of optimum printing settings, samples printed with non-optimal settings are also printed and measured. To demonstrate the influence of resultant relative permittivity of printed antenna materials on the radiation characteristics, a dielectric lens (LWA) is chosen [15]. LWA is redesigned with both materials printed with optimal and non-optimal settings. Radiation characteristics of designed antennas are analyzed by CST Microwave Studio based on finite-integration technique. To the best of our knowledge, although electrical properties of the antenna material are a critical issue in broadband lens antenna designs, such an investigation has not been studied in literature for additively manufacturing.

2. 3D PRINTING PROCESS

Preperm ABS1000 filament of 1.75 mm diameter was used for the 3D printing of antenna core and perforated samples. It is a composite material that contains ceramic nanoparticles in ABS matrix which is a light and hard polymeric material with a relatively high melting point and high durability. It is commonly used in FFF technology. The addition of ceramic nanoparticles provides relatively high and stable dielectric constant and very low tangent loss. Preperm ABS1000 is a white filament with a density of 2200 kg/m^3 and has a water absorption capacity of 0.3% (EN ISO 62:2002). According to the manufacturer, the material provides a loss tangent value as low as $\tan\delta = 0.003$ and a stable dielectric constant ($\varepsilon_r = 10 \pm 0.35$) over a wide frequency band and temperature.

To observe the frequency-dependent electrical permittivity characteristics of the filament, test samples with 22.84 mm × 10.15 mm (width × height) size were printed. The thickness of test samples was set to 1.75 mm since the measurement of dense dielectric materials requires thin samples to prevent inaccurate results [28]. The filament was preconditioned at 90°C for 5 hours to remove moisture. 3D printing process was accomplished by a core XY-type fused deposition modeling (FDM) printer. The printer is equipped with an inductive bed leveling sensor and offers real-time compensation. It was upgraded with an original full-metal hot-end and 0.4 mm stainless-steel nozzle since brass nozzles are not commonly used with abrasive filaments like ceramic-filled ones. Besides, a direct, dual-drive extruder was also mounted on the printer to keep constant flow and minimize clogging of the nozzle due to inadequate feeding of the material. Since the material tends to warp during a rapid cooling process, the cooling fans were kept off during printing to minimize the warping of the printed samples around corners and edges. For the same purpose, an acrylic cover was also used to keep the temperature relatively constant inside the printing chamber and reduce temperature gradient relatively small. It should be noted that warping of the ABS material can be prevented by using industrial-grade 3D printers with chamber-heating features. The printing process has been accomplished over a magnetic plate covered with a blue 3D printing tape (3M$^{\text{TM}}$) at 100°C. For all prints, extrusion width was 110% (0.44 mm) with a layer height of 0.3 mm in the first layer. The first layer printing speed was 10 mm/s. Repetier software with CuraEngine was used to produce g-code for 3D prints. The printing settings in Table 1 were used to produce a total of 48 sample prints with three printing process temperatures, four printing speeds, and four layer heights. All printed test samples are listed with a unique code that contains the temperature, speed, and layer height of the print. For instance, the sample 230S20L15 is the one that is printed at 20 mm/s and 230°C with a layer height of 0.15 mm.

By inspecting the printed samples, it was observed that using a relatively high process temperature at 230–240°C performed well and allowed to print samples without any visible defects. Some of selected printed samples are shown in Fig. 1. Among the samples, 240S20L15 was the most successfully printed one with a smooth surface and no visible air gaps. The second and third samples were printed at 230°C. While a reasonable quality was achieved with a printing speed of 30 mm/s (230S30L20), several defects were formed on the surface of 230S40L15 mainly due to poor interlayer bonding between layers. Besides, air gaps may result from extensive shrinkage of the printed sample due to rapid cooling process. The
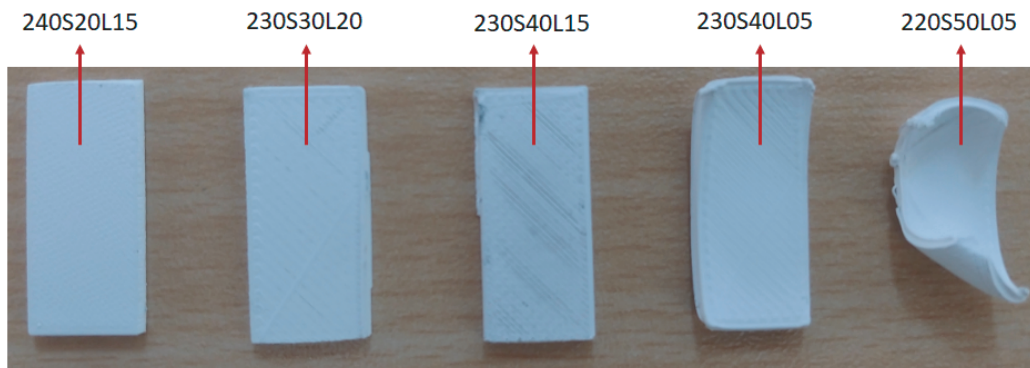

Figure 1. 3D printed test samples using various printing settings.

Table 1. Printing settings for test samples.

Filament Settings	
Flow	100%
Hotend temperature	220, 230, 240°C
Bed temperature	100°C
Fan speed	0% (off)
Printing Settings	
Speed	
Travel	100 mm/s
First layer	10 mm/s
Outer perimeter	Equal to printing speed
Inner perimeter	Equal to printing speed
Infill	Equal to printing speed
Skin infill	Equal to printing speed
Printing speed	20, 30, 40, 50 mm/s
Structure	
Shell thickness	0.8 mm (2 lines)
Top/bottom thickness	0.8 mm
Retraction	
Speed	40 mm/s
Length	1.5 mm
Layers	
First layer height	0.3 mm
First layer line width	0.44 mm (110%)
Layer height	0.05, 0.10, 0.15, 0.20
Infill	100%

presence of such defects (air gaps) may lead to a considerable reduction of the relative permittivity of manufactured final products. The fourth test sample (230S40L05) in Fig. 1 was printed with the same process temperature and speed as the third sample except for layer height (0.05 mm). This setting resulted in an unworkable printed sample since the edges were warped considerably as shown in Fig. 1. In addition to the well-known warping characteristics of any ABS material, the lower layer height is also considered to be another factor that contributes to the warping of printed sample due to increased shear effect created by the pressure of print-head (hot-end) over the printed sample. The last test sample in Fig. 1 was printed at 220°C and 50 mm/s with 0.05 mm layer height, which was a complete failure due primarily to inadequate adhesion to the build plate and extensive warping.

Visual inspection on printed samples pointed out that the most satisfying results were obtained with high process temperatures, low printing speeds, and moderate layer heights. On the other hand, very small layer heights contribute to the warping of printed samples. Besides, high printing speeds lead to air gaps [26]. Furthermore, low temperatures weaken the adhesion force between the printed sample and the build plate, which also contributes to warping effect. Considering the quality of printed samples, one can conclude that printing temperature around 230–240°C, printing speed less than 30–35 mm/s, and a layer height around 0.15 mm (for a nozzle diameter of 0.4 mm) are good printing settings for high quality prints with Preperm ABS1000 filament.

2.1. Measurement of Printed Test Samples

Determining dielectric properties of materials at microwave frequencies is critical for antenna and microwave circuit designers. This valuable information aids in improving design precision. Accurate measurement of dielectric properties provides a significant advantage that has an influence upon radiation characteristics of dielectric filled antennas. With this aim, numerous measurement methods that can be classified as resonant and non-resonant methods are developed [29–32].

In this paper, we use the rectangular waveguide method which is a widely used transmission/reflection method to measure transmitted and reflected electromagnetic waves. The transmission phase-shift (TPS) method is utilized for extracting dielectric properties of test samples from X-band rectangular waveguide measurement results. This method is independent of test sample position inside the waveguide in estimating complex permittivity value. The relative electrical permittivity of dielectric material is a complex quantity given in Eq. (1):

$$\varepsilon_r = \varepsilon_r' - j\varepsilon_r'' \tag{1}$$

Real part in Eq. (1) is related to stored energy by the material from an external electric field where imaginary part is related to dissipated energy. In TPS method, the complex permittivity of test material can be expressed as [32]:

$$\varepsilon_r' = \frac{1}{k_0^2}\left\{\left(\gamma_0 + \frac{\phi_{air} - \phi_{sample}}{d}\right)^2 + \left(\frac{\pi}{a}\right)^2 - \alpha^2\right\} \tag{2a}$$

$$\varepsilon_r'' = \frac{2\alpha}{k_0^2}\left\{\gamma_0 + \frac{\phi_{air} - \phi_{sample}}{d}\right\} \tag{2b}$$

where k_0 is the wave number in free-space. a and d are the aperture width of the waveguide and thickness of test sample, respectively. ϕ_{air} is measured phase of delivered electromagnetic wave at the second port when the waveguide is air-filled (without test sample), and ϕ_{sample} is measured phase when test sample is placed into the waveguide. The propagation constant, γ_0, in rectangular waveguide can be given as follows:

$$\gamma_0 = \sqrt{k_0^2 - \left(\frac{\pi}{a}\right)^2} \tag{3}$$

The attenuation constant, α, (neper/m) in Eq. (2a) can be expressed as:

$$\alpha \cong -1.15129\left\{\frac{1}{d}\log_{10}|S_{11\_sample}|^2 + |S_{21\_sample}|^2 - \frac{1}{d_w}\log_{10}|S_{11\_air}|^2 + |S_{21\_air}|^2\right\} \tag{4}$$

S_{11_air} and S_{21_air} are measured reflection and transmission coefficients without test samples where S_{11_sample} and S_{21_sample} are measured coefficients with test samples inside the waveguide. Finally, d_w is the length of X-band rectangular waveguide.

2.2. Measurement Setup

Dimensions of test samples should prevent air gaps between samples and waveguide since they have potential to affect dielectric constant measurements. Printed samples were measured using a digital caliper to ensure dimensional accuracy of the prints. Measurement results showed that the samples were printed with excellent dimensional accuracy with average errors of 0.45% on the long side and 0.4% on the short side. Thus, samples fit precisely to the X-band rectangular waveguide aperture. Magnitudes of reflection, transmission coefficients, and phase shift amounts were measured with the setup exhibited in Fig. 2(a) together with the VNA, waveguide adaptors, and 4 cm long customized waveguides. Although TPS is a test sample position independent method, test samples were placed inside a flange between the waveguides. Thru-reflect-line (TRL) calibration was applied to set the plane of incident and reflected electromagnetic waves on the surfaces of test samples as given in Fig. 2(b).

Relative electrical permittivity values of 48 test samples are measured. The variation of measured relative permittivity values of printed samples with frequency is given in Fig. 3. The highest values were obtained at 240°C process temperature. As given in Fig. 3, the ε_r value of 240S20L15 was almost equal
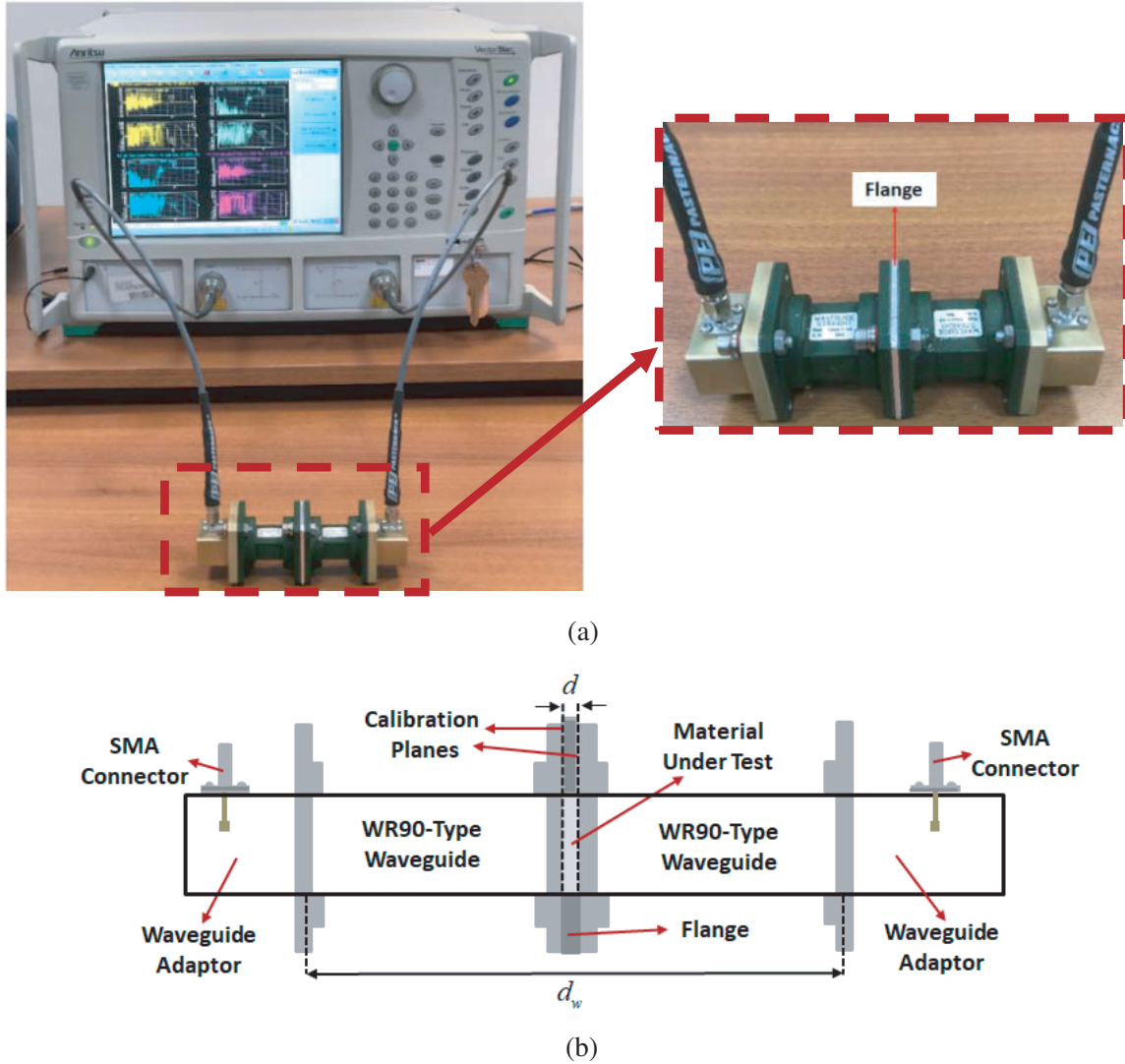
(a)

(b)

Figure 2. Experimental set up for scattering parameter measurements. (a) A flange with a test sample is placed between X-band rectangular waveguides. (b) Cross-section of the waveguides with a test sample of d thickness. Calibration planes are also presented.

to 10 at 8.2 GHz. This value decreased to 9.4 at the highest frequency. The decrease of ε_r at higher frequencies can be associated with the air gaps between layers. These air gaps become more parasitic with increase of frequency. The ε_r values of samples printed with other settings at this temperature decrease more rapidly. An example for such a situation is also exhibited for sample 240S30L10. Test samples printed at 230°C have some visible defects as given in Fig. 1. Thus, the highest ε_r values of these test samples are measured around 8.5 in X-band. The ε_r value of 230S40L05 is a bit lower since its edges were bent. Test samples printed at 220°C resulted in the lowest ε_r values. An example of ε_r variation for 220S40L15 is also presented in Fig. 3. Considering ε_r variations of all printed samples, parameters of 240°C process temperature, 20 mm/s printing speed, and 0.15 mm layer height were determined as the ideal printing settings. The measured loss tangent values of printed test samples were in the range of 0.005–0.007 and in an agreement with the datasheet of manufacturer.

Table 2 shows the comparisons of our proposed printing procedure with the published works in which the same high-permittivity composite material is used for printing. These results exhibit that by carrying out a comprehensive 3D printing process, relative permittivity values closest to manufacturer's datasheet are obtained in our work.
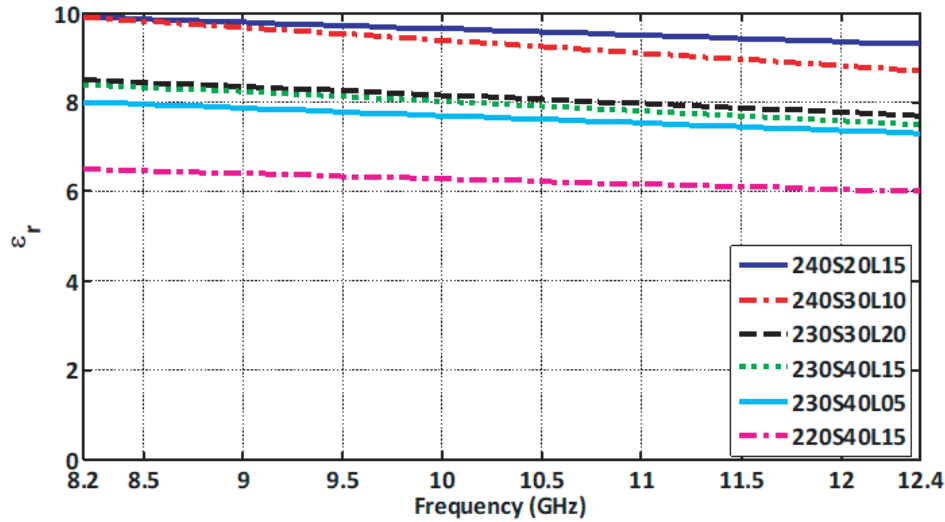
Figure 3. Measured ε_r values of selected test samples in X-band.

Table 2. Comparison of proposed printing procedure with references.

Reference	Printing parameters			frequency (GHz)	ε_r		$\tan\delta$ (measured)
	temperature (°C)	layer height (mm)	speed (mm/s)		measured	expected	
[25]	fast settings	fast settings	fast settings	7–12.4	8.3	10 ± 0.35	-
[26]	260	0.4	20	10	9.06 ± 0.09	10 ± 0.35	0.03
[27]	240	0.2	80	10	9.64 ± 0.016	10 ± 0.35	0.003
Present paper	240	0.15	20	8.2–12.4	9.5–10	10 ± 0.35	0.007

2.3. Advantages of AM in Dielectric ML Fabrication

In the traditional fabrication process of LWA, the lens shape was constructed with printed circuit board technology using a high dielectric RogersTMM10i material sheet as given in Fig. 4(a). Dielectric structure includes three different materials as the MLs. ML materials were chosen considering broadband impedance matching demands. Rogers TMM6 ($\varepsilon_r = 6.3$), Rogers TMM4 ($\varepsilon_r = 4.7$), and Rexolite ($\varepsilon_r = 2.54$) were used as inner, middle, and outer ML materials, respectively. The thicknesses of the MLs from the inside out are calculated using the cascaded transmission line model [8] as 3.57 mm, 5.3 mm, and 7.59 mm. ATheplanar lens structure consists of metallic plates on both sides. The parallel plate waveguide structure was composed of a combination of a semi-circular part with radius $R = 80.5$ mm and a rectangular part $E = 0.35 \times R$. Rectangular extension is added to obtain the elliptical profile. The thickness of elliptical dielectric structure, h, equals 5.08 mm.

Due to the bonding process of MLs to antenna core material, sticky surfaces and possible parasitic air gaps may occur, and this increases the intensity of internal reflections. An alternative solution is drilling holes with a diameter smaller than wavelength in ML regions using CNC machines as proposed in [18]. It is stated in [17] that while the goal was obtaining effective relative permittivity, ε_{eff} value of 2.54 at the outer ML region, 3.2 was obtained using a square lattice as given in Fig. 5. This value can be reduced by drilling more air holes. However, high permittivity dielectric slabs that contain ceramic
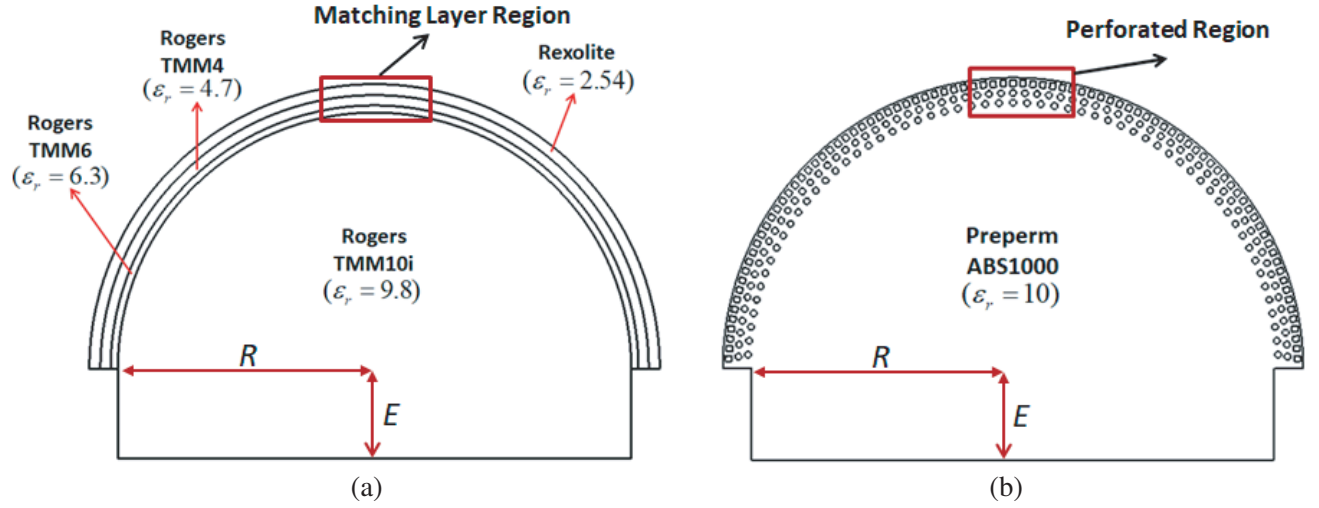
Figure 4. Dense dielectric elliptical antenna core [15] with (a) three MLs, (b) perforations.
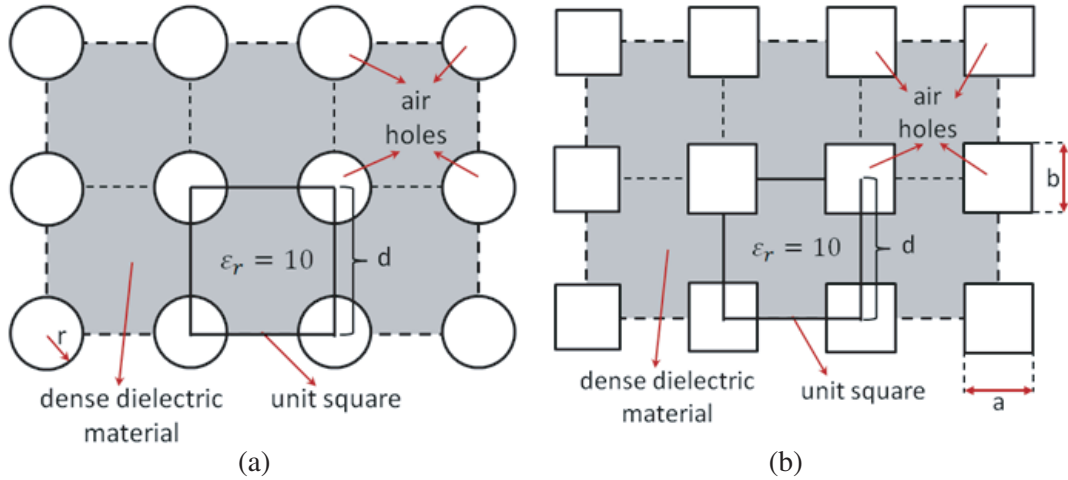

Figure 5. Dielectric test sample structures with (a) circular, (b) rectangular perforations.

nanoparticles are fragile and increase the number or diameter of holes reduces the mechanical strength.

In this work, AM is proposed for fabrication of the LWA using a dense dielectric material, Preperm ABS1000 with relative permittivity of $\varepsilon_r = 10$. The dielectric ML regions of the antenna can be fabricated with perforated regions as given in Fig. 4(b). Achieving desired ε_{eff} values at ML regions of dielectric part is possible by printing the dense dielectric material with necessary perforations. Here, the usage of a single dense material will be sufficient instead of four and internal reflections due to sticky surfaces, and air gaps will be eliminated.

2.4. Perforated Sample Fabrication

In a 3D printing process, ε_{eff} of a material can be reformed by controlling the number and dimensions of air holes [33, 34]. In this work, the perforations on test samples are employed as uniform square lattices with circular and rectangular shapes as given in Figs. 5(a) and (b), respectively. Rectangular air perforations which cannot be obtained in a traditional fabrication process are implemented to outer ML region to achieve a higher air/material volume ratio and consequently, lower ε_{eff} value.

A static model is used to predict the value of ε_{eff} based on area volume ratio of the perforation

lattices. In the given square lattices, ε_{eff} of each ML region can be estimated by the following equation:

$$\varepsilon_{eff} = \varepsilon_{r_1} f_1 + \varepsilon_{r_2} f_2 \tag{5}$$

where f_1 and f_2 are the volume fractions of air and dielectric material, respectively. Note that $f_1 + f_2 = 1$. ε_{r_1} is the relative permittivity of air, and ε_{r_2} is the relative permittivity of dielectric material ($\varepsilon_{r_2} = 10$). In our application, f_1 and f_2 are considered as area fractions on ML regions since thickness, h, of the material is homogeneous through the elliptical antenna. Thus, f_1 can be defined as $\pi r^2/d^2$ for the square lattice of circular holes. For rectangular perforations, f_1 should be modified as ab/d^2.

As mentioned, relative permittivity values of employed MLs are 6.3, 4.7, and 2.54 from inside out, respectively. In order to achieve the $\varepsilon_{eff} = 6.3$ value in the inner ML region, 0.4 volume fraction of air should be formed. Similarly, using Eq. (5) it can be calculated that 0.58 and 0.83 volume fractions of air are required to obtain $\varepsilon_{eff} = 4.7$ and $\varepsilon_{eff} = 2.54$ for the middle and outer ML regions, respectively. The dimensions of required test samples for each ML region are given in Fig. 6 together with dimensions of perforations on their surfaces. Here, L and W are equal to 22.84 and 10.15 mm, respectively. The lower ε_{eff} value for the second ML region is achieved with larger air holes. In order to obtain the desired low ε_{eff} value for the outer ML, 0.83 volume fraction of air is achieved with rectangular perforations.
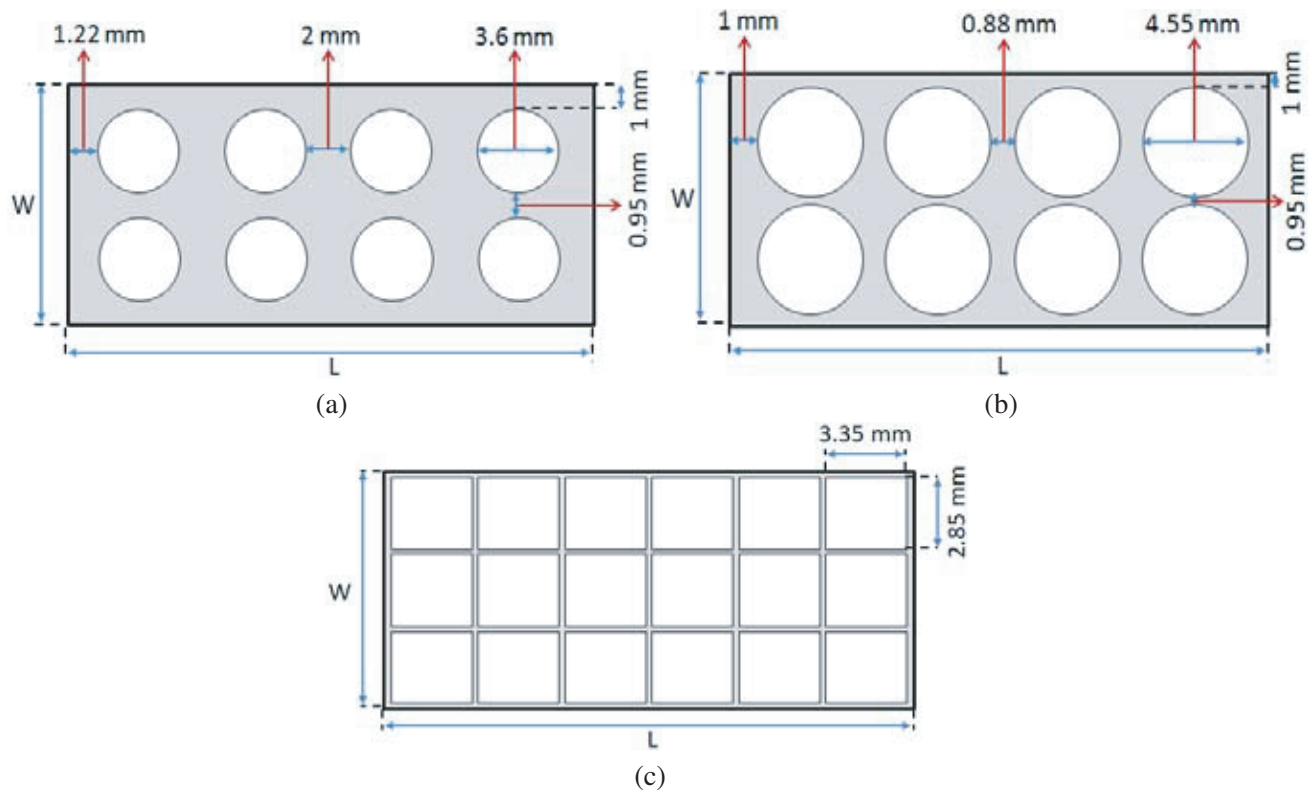

Figure 6. The dimensions of fabricated test samples. (a) Inner ML. (b) Middle ML. (c) Outermost ML.

Six perforated test samples are printed. In the AM process of the first three samples, determined ideal printing settings were used. Printed samples are given in Fig. 7. The rest of the samples are printed with non-optimum printing settings of 230°C process temperature, 40 mm/s printing speed, and 0.05 mm layer height. It is exhibited in Fig. 3 that samples printed with these non-optimum settings have a lower ε_{eff} value than the expected value of 10. These samples are printed to exhibit the influence of non-optimum printing parameters on resultant ε_{eff} values.

ε_{eff} values of test samples are measured with the experimental setup given in Fig. 2(a). Measured ε_{eff} values of all perforated samples are given in Fig. 8. It can be concluded that desired ε_{eff} values of the ML regions are closely achieved with test samples printed using ideal setting parameters. Besides, these
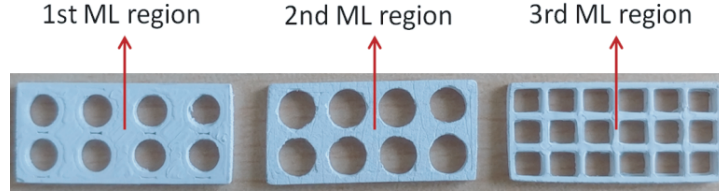
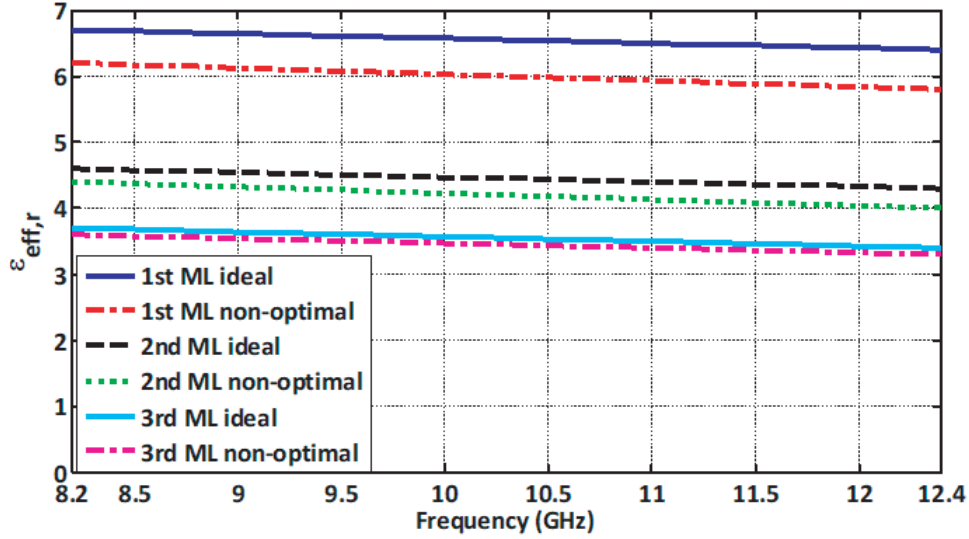**Figure 7.** The test samples printed for ML regions with ideal settings.

Figure 8. Measured ε_{eff} variations of printed test samples with frequency. Test samples are printed with ideal and non-optimal settings.

values are almost stable over X-frequency band. As shown in Fig. 8, ε_{eff} values of samples printed with non-optimal settings are noticeably lower than relative permittivity values of ML regions, especially for the inner ML.

3. INFLUENCE OF MATERIAL ε_r VALUES ON THE ANTENNA RADIATION CHARACTERISTICS

The impact of 3D printing process parameters on the resultant relative permittivity values of dense dielectric materials has been presented. In this section, the influence of relative permittivity values of dielectric parts on the radiation characteristics of the LWA is investigated. Three different antenna structures are considered. All the antennas consist of two perfectly conducting planar waveguides that sandwich the dielectric lens part. Dielectric part of the first antenna is assumed to be manufactured using printed circuit board (PCB) technology. It is constructed with an ellipse core and circular crown ML profiles as given in Fig. 9(a). Other two antenna structures are assumed to be manufactured using 3D printing process. Thus, the upper part of their lens structure is designed by the perforated structures. In this way, antenna cores are coated with necessary perforations as shown in Fig. 9(b). While one of the additively manufactured antennas is considered to be printed with ideal settings, the other one is assumed to be printed with non-optimal settings.

It should be noted that in the traditional method, the manufacturing processes of dielectric antenna core and MLs are presumed to be completed in ideal conditions. Thus, parasitic air gaps which will remain between antenna core and coating materials during fabrication are neglected. Simulations are performed by using time domain solver of CST Microwave Studio. In Fig. 10, simulated S_{11} variations of all designs are presented. As shown, antennas with traditionally fabricated dielectric parts and
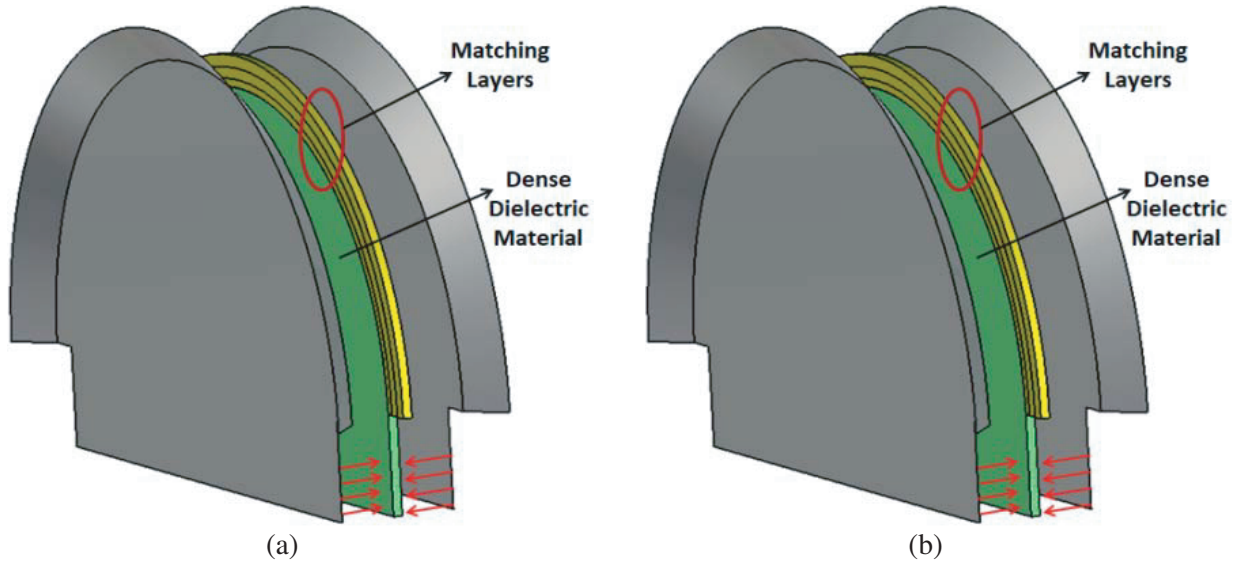
Figure 9. Dielectric loaded lens antennas designed for (a) traditional manufacturing process, (b) 3D printing process.
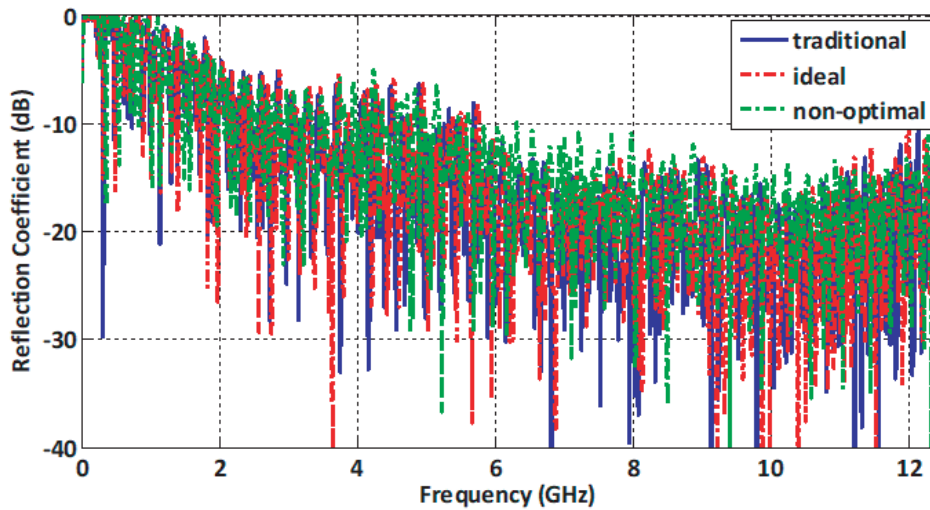

Figure 10. Simulated S_{11} responses of the antennas.

fabricated with perforations considering ideal printing settings exhibit a good correspondence in S_{11} characteristics in X-band. However, the antenna whose perforations are formed with non-optimal settings has a slightly higher S_{11} value. This can be explained with higher reflections due to the lower relative permittivity values of perforated region than expected.

Realized gain variations of three antennas are demonstrated in Fig. 11 as the function of frequency. It is observed that traditionally manufactured and 3D printed antennas with ideal settings will exhibit comparable realized gain variations in the whole frequency band. The realized gain value of a traditionally fabricated antenna will vary between 18 and 20 dBi. Similarly, the antenna printed with ideal settings will have realized gain value between 17 and 20 dBi. Although the realized gain of the antenna printed with ideal settings will be 1.5 dBi lower than a traditionally fabricated antenna at 8 GHz, the realized gains of both antennas are almost stable up to 12 GHz. The realized gain variation of the antenna printed with non-optimum settings will be approximately 4 dB lower than the antenna printed with ideal settings in the whole operation frequency band.
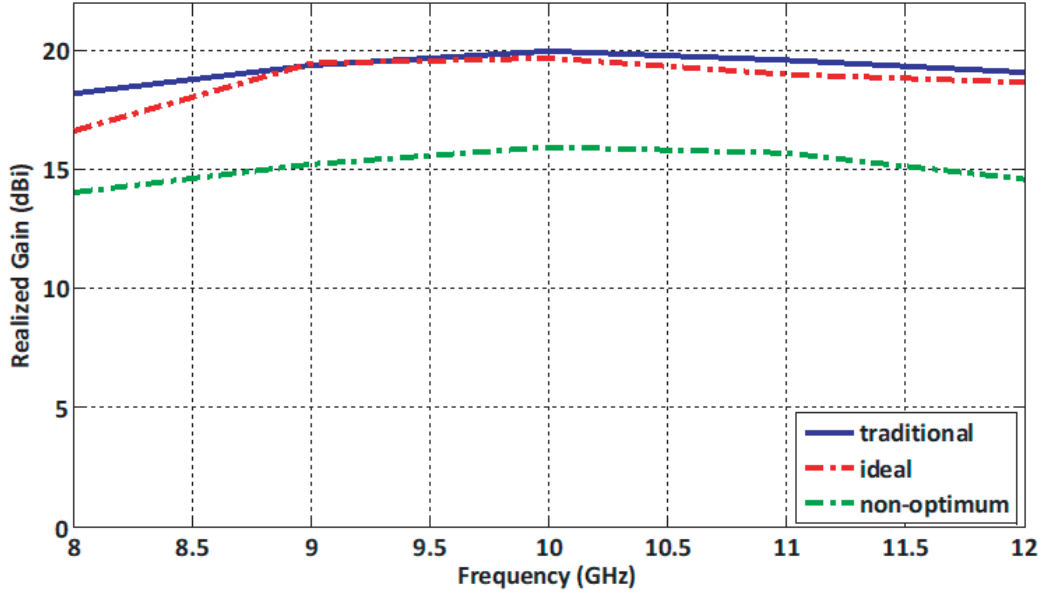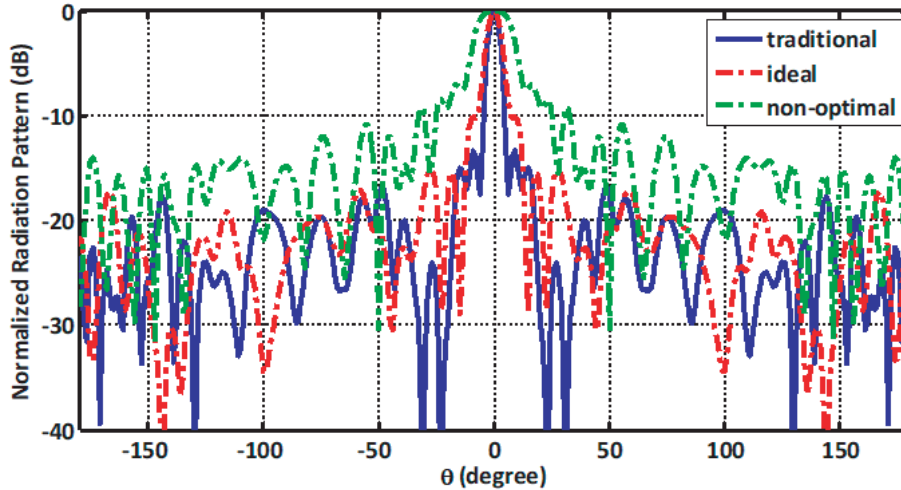
Figure 11. Realized gains of dielectric loaded antennas with frequency.

In Figs. 12(a) and (b), simulated radiation patterns of the antennas are presented in $\emptyset = 0°$ plane at 8 and 12 GHz, respectively. It is clear that radiation patterns of the antennas manufactured with traditional method and 3D printing with proposed ideal settings are very close. However, half power beamwidth of the antenna fabricated with non-optimal printing settings is dramatically higher. Especially at 12 GHz, main beam of the antenna splits into two and does not radiate to boresight. The deterioration of antenna radiation can be explained as that the focal length of a dielectric lens is very sensitive to changes in the ε_r of core material since rectangular extension E given in Fig. 4 is defined as $D/2\sqrt{\varepsilon_r}$. When the lens antenna is printed using non-optimal printing settings, relative permittivity values of antenna core and perforated regions result in lower permittivity values than expected due to air voids between layers.

In Figs. 13(a) and (b), simulated radiation patterns of the antennas in $\emptyset = 90°$ plane are presented at 8 and 12 GHz. In Fig. 13, a good correspondence is observed between radiation characteristics of additively manufactured antenna with ideal printing settings and traditionally fabricated antenna. A 3D printed antenna with non-optimal settings will exhibit higher half power beamwidth characteristics
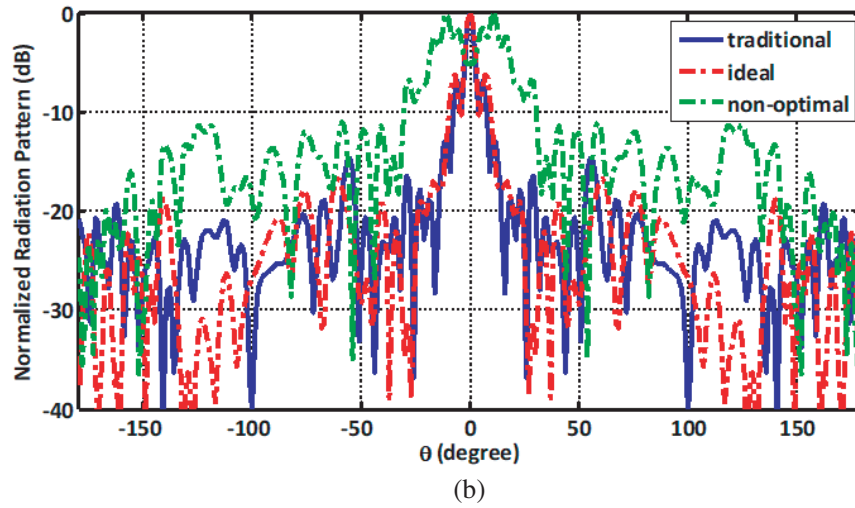

(a)

(b)

Figure 12. Normalized radiation patterns of dielectric loaded lens antennas in $\emptyset = 0°$ plane at (a) 8 and (b) 12 GHz.
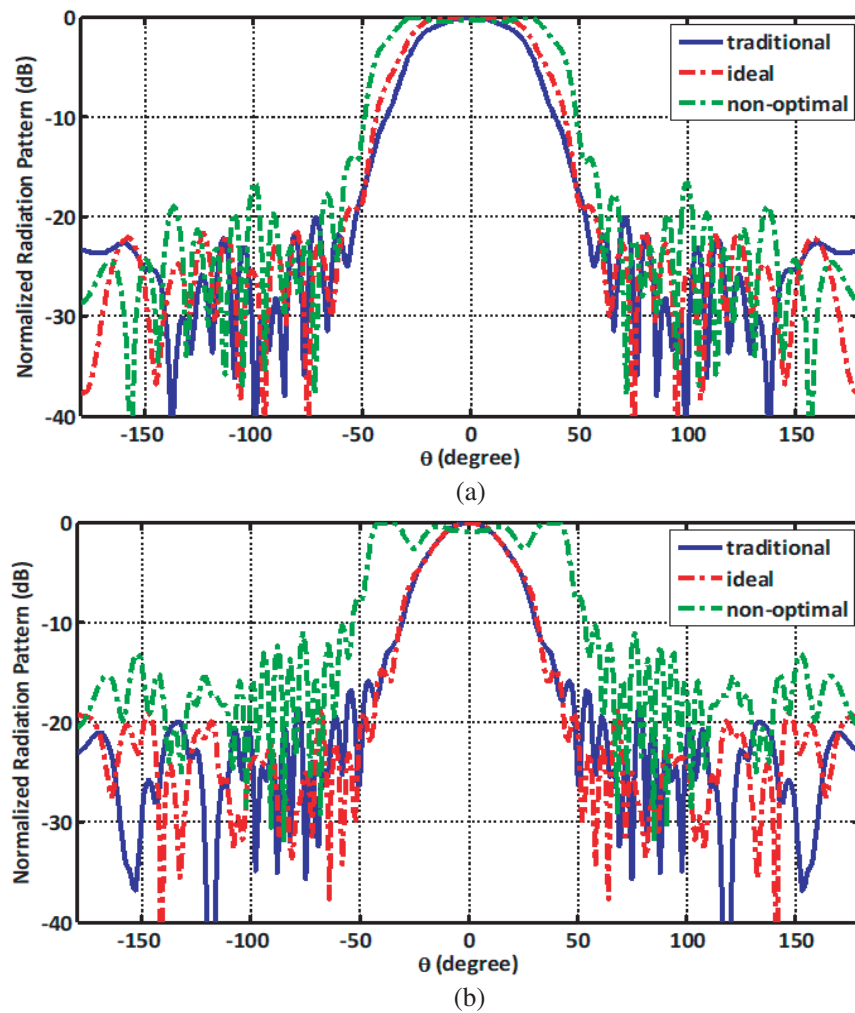

(a)

(b)

Figure 13. Normalized radiation patterns of dielectric loaded lens antennas in $\emptyset = 90°$ plane at (a) 8 GHz and (b) 12 GHz.

than traditionally fabricated antenna also in this plane. At 12 GHz, radiation pattern of the antenna splits into two beams; each radiating to undesirable directions. This can be explained as that the perforated regions printed with non-optimal settings do not play the critical role of MLs in reducing the strong internal reflections due to the resulting unexpected $\varepsilon_{eff,r}$ values in this region. The sidelobe level of the antenna printed with ideal settings will be slightly higher than traditionally fabricated antenna at 12 GHz in both planes as seen in Figs. 12(b) and 13(b). This can be explained by the decrease of measured ε_r values of printed samples with frequency as given in Figs. 3 and 8.

4. CONCLUSION

In this work, 3D printing technology is proposed for manufacturing dense dielectric loaded lens antennas. Utilizing favorable printing settings during printing process is crucial since main process parameters have a high impact on dielectric properties of resulted antenna material. Preperm ABS1000 is used to print samples for dielectric core and perforated regions with high permittivity and low-loss thermoplastic material. Forty-eight test samples are printed for the lens core, and dielectric properties of these samples are measured using a VNA. Measured relative electrical permittivity values of samples show that process temperature should be at least 240°C to achieve a successful printing. To avoid warping around corners and edges of printings, printing speed of less than 30–35 mm/s and layer height of around 0.15 mm should be employed. Besides, three test samples with perforations are printed with ideal settings where the other three samples are printed with non-optimal settings. It is observed that desired ε_{eff} values are almost achieved for samples printed with perforations using ideal settings.

The impact of perforated regions designed compatible with AM technique on dielectric loaded lens antenna radiation characteristics is investigated and compared with traditional method. Simulation results clearly show the reliability of perforated structures as MLs and importance of using ideal printing settings in AM process. It is exhibited that an additively manufactured dense dielectric lens antenna would have the performance of a traditionally manufactured dielectric antenna if and only if it is manufactured with optimum printing parameters. In this case, the AM process of dielectric loaded lens antennas performed with ideal settings will provide significant advantages to design flexibility, compactness, fast and low-cost prototyping compared to traditional fabrication methods. Since the recommended minimum wall thickness value between perforations is 1.5 mm for ABS materials, the radiation characteristics of a perforated high dielectric lens antenna printed with today's 3D printing technology will degrade in the upper range of mmWave frequency band.

REFERENCES

1. Filipovic, D. F., S. S. Gearhart, and G. M. Rebeiz, "Double-slot antennas on extended hemispherical and elliptical silicon dielectric lenses," *IEEE Transactions on Microwave Theory and Techniques*, Vol. 41, No. 10, 1738–1749, Oct. 1993.
2. Costa, J. R., C. A. Fernandes, G. Godi, R. Sauleau, L. Le Coq, and H. Legay, "Compact Ka-band lens antennas for LEO satellites," *IEEE Transactions of Antennas and Propagation*, Vol. 56, No. 5, 1251–1258, May 2008.
3. Pasqualini, D. and S. Maci, "High-frequency analysis of integrated dielectric lens antennas," *IEEE Transactions of Antennas and Propagation*, Vol. 52, No. 3, 840–847, Mar. 2004.
4. Schoenlinner, B., X. Wu, J. P. Ebling, G. V. Eleftheriades, and G. M. Rebeiz, "Wide-scan spherical-lens antennas for automotive radars," *IEEE Transactions on Microwave Theory and Techniques*, Vol. 50, No. 9, 2166–2175, Sept. 2002.
5. Ettorre, M., R. Sauleau, L. Le Coq, and F. Bodereau, "Single-folded leaky-wave antennas for automotive radars at 77 GHz," *IEEE Antennas and Wireless Propagation Letters*, Vol. 9, 859–862, Sept. 2010.
6. Yang, L., C. W. Domier, and N. C. Luhmann, "Q band to V-band 1D and 2D elliptical lens antenna arrays," *Microwave and Optical Technology Letters*, Vol. 49, No. 8, 1798–1801, Aug. 2007.

7. Nguyen, N. T., R. Sauleau, and C. J. M. Pérez, "Very broadband extended hemispherical lenses: Role of matching layers for bandwidth enlargement," *IEEE Transactions of Antennas and Propagation*, Vol. 57, No. 7, 1907–1913, Jul. 2009.

8. Tokan, F., "Optimization-based matching layer design for broadband dielectric lens antennas," *ACES Journal*, Vol. 29, No. 6, 499–507, Jun. 2014.

9. Sönmez, N. T. and N. T. Tokan, "Effects of anti reflective coatings on scanning performance of millimetre-wave lenses," *IET Microw. Antennas Propag.*, Vol. 10, No. 14, 1485–1491, Nov. 2016.

10. Yang, F., X. Wu, J. Zhou, and H. Shao, "Beam-scanning lens antenna based on corrugated parallel-plate waveguides," *IEEE Antennas and Wireless Propagation Letters*, Vol. 17, No. 7, 1296–1299, Jul. 2018.

11. Monkevich, J. M. and G. P. Le Sage, "Design and fabrication of a custom-dielectric Fresnel multi-zone plate lens antenna using additive manufacturing techniques," *IEEE Access*, Vol. 7, 61452–61460, May 2019.

12. D'Auria, M., et al., "3-D printed metal-pipe rectangular waveguides," *IEEE Transactions on Components, Packaging and Manufacturing Technology*, Vol. 5, No. 9, 1339–1349, Sept. 2015.

13. Syed, W. H., D. Cavallo, H. T. Shivamurthy, and A. Neto, "Wideband, wide-scan planar array of connected slots loaded with artificial dielectric superstrates," *IEEE Transactions on Antennas and Propagation*, Vol. 64, No. 2, 543–553, Feb. 2016.

14. Neto, A., "UWB, non-dispersive radiation from the planarly fed leaky lens antenna — Part I: Theory and design," *IEEE Transactions of Antennas and Propagation*, Vol. 58, No. 7, 2238–2247, Jul. 2010.

15. Tokan, F., N. T. Tokan, A. Neto, and D. Cavallo, "The lateral wave antenna," *IEEE Transactions on Antennas and Propagation*, Vol. 62, No. 6, 2909–2916, Jun. 2014.

16. Patel, P., B. Mukherjee, and J. Mukherjee, "A compact wideband rectangular dielectric resonator antenna using perforations and edge grounding," *IEEE Antennas and Wireless Propagation Letters*, Vol. 14, 490–493, Nov. 2014.

17. Tokan, F., D. Cavallo, and A. Neto, "A novel planar, broadband, high gain lateral wave antenna array for body scanning applications," *Journal of Electrical Engineering*, Vol. 71, No. 5, 308–316, Oct. 2020.

18. Al-Nuaimi, M. K. T. and W. Hong, "Discrete dielectric reflectarray and lens for E-band with different feed," *IEEE Antennas and Wireless Propagation Letters*, Vol. 13, 947–950, Mar. 2014.

19. Mahouti, P., F. Güneş, M. A. Belen, and A. Çalışkan, "A novel design of non-uniform reflectarrays with Symbolic Regression and its realization using 3-D Printer," *ACES Journal*, Vol. 34, No. 2, Feb. 2019.

20. Bjorgaard, J., M. Hoyack, E. Huber, M. Mirzaee, Y.-H. Chang, and S. Noghanian, "Design and fabrication of antennas using 3D printing," *Progress In Electromagnetics Research C*, Vol. 84, 119–134, May 2018.

21. Parsons, P., Z. Larimore, F. Muhammed, and M. Mirotznik, "Fabrication of low dielectric constant composite filaments for use in fused filament fabrication 3D printing," *Additive Manufacturing*, Vol. 30, 1–10, Jan. 2020.

22. Ghazali, M. I. M., S. Karuppuswami, A. Kaur, and P. Chahal, "3D printed high functional density packaging compatible out-of-plane antennas," *Additive Manufacturing*, Vol. 30, 1–7, Dec. 2019.

23. Zhang, S., "Three-dimensional printed millimetre wave dielectric resonator reflectarray," *IET Microw. Antennas Propag.*, Vol. 11, No. 14, 2005–2009, Oct. 2017.

24. Zhang, S., R. K. Arya, S. Pandey, Y. Vardaxoglou, W. Whittow, and R. Mittra, "3D-printed planar graded index lenses," *IET Microwaves, Antennas & Propagation*, Vol. 10, No. 13, 1411–1419, Oct. 2016.

25. Huang, J., S. J. Chen, Z. Xue, W. Withayachumnankul, and C. Fumeaux, "Wideband endfire 3-D-printed dielectric antenna with designable permittivity," *IEEE Antennas and Wireless Propagation Letters*, Vol. 17, No. 11, 2085–2089, Nov. 2018.

26. Goulas, A., et al., "The impact of 3D printing process parameters on the dielectric properties of high permittivity composites," *Designs*, Vol. 3, No. 50, 1–10, Nov. 2019.

27. Goulas, A., S. Zhang, J. R. McGhee, D. A. Cadman, W. G. Whittow, J. C. Vardaxoglou, and D. S. Engstrøm, "Fused filament fabrication of functionally graded polymer composites with variable relative permittivity for microwave devices," *Materials & Design*, Vol. 193, Aug. 2020.

28. Trabelsi, S., A. W. Kraszewski, and S. O. Nelson, "Phase-shift ambiguity in microwave dielectric properties measurements," *IEEE Transactions on Instrumentation and Measurement*, Vol. 49, No. 1, 56–60, Feb. 2000.

29. Sheen, J., "Study of microwave dielectric properties measurements by various resonance techniques," *Measurement*, Vol. 37, No. 2, 123–130, Mar. 2005.

30. Lee, C. K., et al., "Evaluation of microwave characterization methods for additively manufactured materials," *Designs*, Vol. 47, No. 3, 1–17, Sept. 2019.

31. Fieber, L., S. S. Bukhari, Y. Wu, and P. S. Grant, "In-line measurement of the dielectric permittivity of materials during additive manufacturing and 3D data reconstruction," *Additive Manufacturing*, Vol. 32, 1–11, Mar. 2020.

32. You, K. Y., "Effects of sample thickness for dielectric measurements using transmission phase-shift method," *International Journal of Advances in Microwave Technology (IJAMT)*, Vol. 1, No. 3, 64–67, Nov. 2016.

33. Petosa, A. and A. Ittipiboon, "Design and performance of a perforated dielectric Fresnel lens," *IEE Proceedings — Microwave Antennas and Propagation*, Vol. 150, No. 5, 309–314, Oct. 2003.

34. Colburn, J. S. and Y. Rahmat-Samii, "Patch antennas on externally perforated high dielectric constant substrates," *IEEE Transactions on Antennas and Propagation*, Vol. 47, No. 12, 1785–1794, Dec. 1999.